International Journal of Precision Engineering and Manufacturing (2019) 20:1333–1346
https://doi.org/10.1007/s12541-019-00131-y

Online ISSN 2005-4602
Print ISSN 2234-7593

REGULAR PAPER

An Automatic Assembly Control Method for Peg and Hole Based on Multidimensional Micro Forces and Torques

Fei Shen[1,2] · Zhengtao Zhang[1] · De Xu[1] · Juan Zhang[2] · Wenrong Wu[2]

Received: 18 June 2018 / Revised: 17 April 2019 / Accepted: 18 April 2019 / Published online: 28 May 2019

Abstract
In this paper, an automatic assembly method for peg and hole based on multidimensional micro forces and torques is developed for satisfying the accurate and lossless assembly requirements. The relationship between the forces and torques from the force sensor and the attitudes deviation of peg and hole is discussed. Moreover, a novel method based on active constraint state for estimating the deviation angles between the peg and the hole through the toques exerted on the sensor is proposed. To achieve automated insertion and minimize the contact forces and torques in the meanwhile during the insertion process, a control strategy for controlling contact forces and torques is proposed by eliminating the position and attitudes deviation interactively. Related assembly experiments are conducted to verify the effectiveness of the proposed approaches.

Keywords Automatic assembly · Micro forces control · Micro torques control

1 Introduction

Micro-assembly is one of the key techniques in the domain of advanced manufacturing, which can be widely applied to the fields of Micro-Electro-Mechanism System (MEMS), precision photo-electronic engineering, biotechnology, medical science, etc. [1–4]. Since the operating objects are small and easily damaged, micro-assembly not only needs microscopic vision to offer essential observation, but demands controlling the contact force during the operation to ensure the lossless as well. Thus, measuring and control technology of micro-force is regarded as one of the important technical supports for assembly tasks to meet accurate and lossless requirements. The research of measuring technology of micro-force mainly focus on the characteristic of micro-force, measuring methods, and sensors, etc. The control of micro-force in micro-assembly mainly involves two kinds of problems: (1) How to control the micro-gripper to grasp the objects stably and release without adhesion? (2) How to control the micro-force produced in the process of assembly to achieve the purpose of nondestructive?

Aiming at above problems, some achievements have been attained. For the former problem, Thompson et al. design ortho-tweezers to perform automated pick and place task of $200\times200\times100$ micron blocks [5]. Tanikawa et al. propose a two-fingered micro gripper which has the capability of maintaining the force between the gripper and a micro ball with 5 μm in size based on the force sensor attached with finger [6]. Kim et al. design a monolithic MEMS-based micro-gripper with integrated force feedback along two axes and present the first demonstration of force controlled micro-grasping at the nanonewton force level [7]. Xu proposes a series of approaches based on sliding mode impendence control to regulate both position and contact force of a piezoelectric-bimorph microgripper for micromanipulation and microassembly applications [8, 9]. Komati et al. propose an automated guiding strategy based on external hybrid force/position control method to manipulate a flexible micro-part [10]. For the latter problem, Zhou et al. investigate the integration use of the microscopic vision and force feedback to perform the impact force control during the assembly [11]. Lu et al. study the issue of force transmission by designing a compound frictionless flexure stage, based on which the interaction force is controlled to follow a desired trajectory [12]. Shen et al. perform the assembly

✉ Zhengtao Zhang
zhengtao.zhang@ia.ac.cn

[1] Research Center of Precision Sensing and Control, Institute of Automation, Chinese Academy of Sciences, Beijing 100190, People's Republic of China

[2] Laser Fusion Research Center, Chinese Academy of Engineering Physics, Mianyang 621900, People's Republic of China

of micro mirror by regulating the micro contact force utilizing a polyvinylidene fluoride (PVDF) force sensor [13]. Li et al. propose a novel method based on the mapping between assembly force and position through a combined error back propagation network and a genetic algorithm. The method is used in the micro-adjustment process to achieve high assembly precision and high assembly quality [14]. Qin et al. present an active radial compliance method based on clustering and support vector machines to perform the insertion task of thin walled millimeter-sized cylinders [15]. Xu proposes the constant-force mechanism to perform micrograpping of biological cells in the pursuit of avioding large deformation which will break the equilibrium state inside the cell [16]. Liu et al. realize high precision assembly of two components in the size of mm level with an interference fit based on microscopic vision and force information [17]. A micro-scale pinhole assembly was analyzed and a shear stress model for repeated interference fits is given considering different pin-tip edges in [18]. Kim et al. propose a shape recognition and a hole detection algorithm based on a 6-axis F/T sensor to realize the precision assembly of peg-in-hole [19].

Although many achievements have been attained in micro-force based micro-manipulation and micro-assembly, the research concerns the automatic 3-D space micro-assembly based on multi-dimensional micro torques are few. The main difficulty lies in that the relationship between the attitude deviation and torque is not the one-to-one mapping relationship due to the uncertain contact state in the process of assembly. One solution for eliminating the attitude deviation without consideration of the uncertain contact state is to make the robot arm, wrist or gripper has certain compliance [20]. However, the limitation of this passive compliant control method is that a larger force may be produced in the assembly process which is absolutely not allowed in many application such as laser target fabrication [21]. In addition, the compliant gripper is also not easy to be fabricated.

Aiming at the above problems, an automatic assembly method for peg and hole insertion based on multidimensional micro forces and torques is developed which can minimize the contact forces and torques in the meanwhile. Firstly, the relationship between the forces and torques from the force sensor and the attitudes deviation of peg and hole is discussed. Moreover, a novel method based on active constraint state is proposed to solve the uncertain relationship between the attitude deviation and torques. On this basis, a control strategy for controlling the horizontal contact forces and torques during the insertion process is designed to achieve automated insertion of peg and hole. Peg and hole micro assembly experiments are conducted to validate the effectiveness of the proposed scheme and the results demonstrate the rationality of proposed approaches.

The rest of the paper is organized as follows. Section 2 analyses the relationship between the forces and torques from the force sensor and the attitudes deviation of peg and hole. Then the method for estimating the deviation angles between the peg and the hole through the force sensor is presented. Section 3 analyzes the control strategy of the automated insertion. Section 4 shows the experiment results and error analysis. Finally, conclusions and suggestions for future work are given in Sect. 5.

2 The Model of Relationship Between the Forces and Torques from the Force Sensor and the Attitudes Deviation of Peg and Hole

2.1 Problem Formulation

The process of peg and hole assembly is generally divided into two stages: (1) the stage of locating the hole; (2) the insertion stage of peg and hole. In the field of micro assembly, micro vision is usually needed to locate micro devices. Therefore, compared with the macro peg and hole assembly, the stage of locating the hole can be directly realized by micro vision, which not only improves the assembly efficiency, but also avoids the damage caused by the searching operation. However, micro vision usually fails in the insertion stage of peg and hole due to occlusion. Meanwhile, for the assembly task of the easily damaged micro part such as thin wall micro part, the forces produced in the insertion stage need to be monitored to ensure the lossless assembly of components.

Since the force or torque produced in the insertion stage is mainly caused by the position and posture deviation of the two parts, it is necessary to solve how to eliminate position and posture deviation based on force or torque information. However, it is difficult to achieve the posture deviation elimination based on torque information since the relationship between them is not the one-to-one mapping relationship due to the uncertain contact state in the process of assembly. To break through this problem, first of all we have to make clear the relationship between the forces and torques from the force sensor and the attitudes deviation of peg and hole.

Thus, the peg and hole insertion method based on six-component force sensor is studied by employing a 7-DOF (degree of freedom) micro-assembly robot whose kinematic scheme is shown in Fig. 1. The robot is able to translate hole $\boldsymbol{A}$ in 3 translational DOF (x, y and z) by utilizing motion platform $\mathbf{W_1}$ and rotate peg $\boldsymbol{B}$ in 3 rotational DOF (θ_x, θ_y and θ_z) in combination of 1 translational DOF (z) in virtue of motion platform $\mathbf{W_2}$ simultaneously. Moreover, a six-component micro force sensor is employed to monitor the

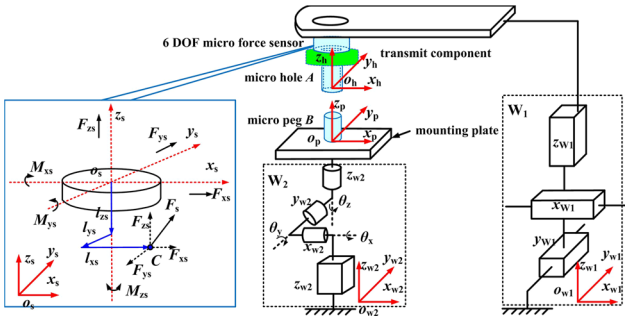

Fig. 1 Kinematic scheme of the micro-assembly robot for peg-hole insertion

forces and torques exerted on the hole $\boldsymbol{A}$. In addition, to express the force, torque, position and pose clearly, three categories of frame should be established first including motor coordinate system, force sensor system and conjoined coordinate system. As shown in Fig. 1, $o_{W1}x_{W1}y_{W1}z_{W1}$ and $o_{W2}x_{W2}y_{W2}z_{W2}$ are motor coordinate systems attached to motion platform $\mathbf{W_1}$ and $\mathbf{W_2}$ respectively with their axes parallel to the stepper motors' moving directions accordingly. $o_sx_sy_sz_s$ is labeled as force sensor coordinate system whose axes coincide with direction of the forces sensing. $o_px_py_pz_p$ and $o_hx_hy_hz_h$ are conjoined coordinate systems attached to peg $\boldsymbol{B}$ and hole $\boldsymbol{A}$ respectively with o_pz_p and o_hz_h are parallel to their axes accordingly.

The general output torque equation of force sensor can be expressed as follows

$$\boldsymbol{M_{xs}} = \boldsymbol{l_{zs}} \times \boldsymbol{F_{ys}} + \boldsymbol{l_{ys}} \times \boldsymbol{F_{zs}} \tag{1}$$

$$\boldsymbol{M_{ys}} = \boldsymbol{l_{zs}} \times \boldsymbol{F_{xs}} + \boldsymbol{l_{xs}} \times \boldsymbol{F_{zs}} \tag{2}$$

$$\boldsymbol{M_{zs}} = \boldsymbol{l_{ys}} \times \boldsymbol{F_{xs}} + \boldsymbol{l_{xs}} \times \boldsymbol{F_{ys}} \tag{3}$$

where $\boldsymbol{F_{xs}}$, $\boldsymbol{F_{ys}}$ and $\boldsymbol{F_{zs}}$ are the forces from the force sensor which are parallel to axes o_sx_s, o_sy_s and o_sz_s respectively. $\boldsymbol{M_{xs}}$, $\boldsymbol{M_{ys}}$ and $\boldsymbol{M_{zs}}$ are the torques exerted on the force sensor which are around the axes o_sx_s, o_sy_s and o_sz_s respectively. $\boldsymbol{l_{xs}}$, $\boldsymbol{l_{ys}}$ and $\boldsymbol{l_{zs}}$ are components of the vector of force arm which is from o_s to contact point $\boldsymbol{C}$ as shown in Fig. 1. Based on the above torque equations, the relationship between the forces and torques from the force sensor and the attitudes deviation of peg and hole is discussed in the following part.

2.2 The Model of Relationship Between the Forces and Torques from the Force Sensor and the Attitudes Deviation of Peg and Hole

The objective of the insertion process can be considered as the adjustments of the position deviation between the peg and the hole axes and the angle between axes of the peg and the hole. Since the case of only position deviation exists is simple, we focus on the analysis for the case of attitudes deviation. When the attitudes deviation exists, there are two types contact situations. One is single point of contact such as the situation of $\mathbf{S_1}$, $\mathbf{S_2}$, $\mathbf{S_4}$ and $\mathbf{S_5}$ shown in Fig. 2, and the other is two-point contact situation as $\mathbf{S_3}$ and $\mathbf{S_6}$.

Before the analysis for the kinds of situations, some notation should be introduced first for the sake of clarity. C_u is labeled as the contact point of the upper surface of the peg and inner side wall of hole. Similarly, C_d denotes the contact point of the lower surface of the hole and the outer side wall of peg. Moreover, $\boldsymbol{F_{xui}}$, $\boldsymbol{F_{yui}}$ and $\boldsymbol{F_{zui}}$ denote the component of resultant force exerted on the contact point C_u along axes o_sx_s, o_sy_s and o_sz_s respectively in the case of $\mathbf{S_i}$ ($i = 1,\ldots 6$). $\boldsymbol{F_{xyui}}$ is the resultant force of $\boldsymbol{F_{xui}}$ and $\boldsymbol{F_{yui}}$. $\boldsymbol{l_{xui}}$, $\boldsymbol{l_{yui}}$, $\boldsymbol{l_{zui}}$ are the components of vector $\overrightarrow{O_sC_u}$ along axes o_sx_s, o_sy_s and o_sz_s respectively. Correspondingly, $\boldsymbol{F_{xdi}}$, $\boldsymbol{F_{ydi}}$ and $\boldsymbol{F_{zdi}}$ denote the component of resultant force exerted on the contact point C_d along axes o_sx_s, o_sy_s and o_sz_s respectively. $\boldsymbol{F_{xydi}}$ is the resultant force of $\boldsymbol{F_{xdi}}$ and $\boldsymbol{F_{ydi}}$. $\boldsymbol{l_{xdi}}$, $\boldsymbol{l_{ydi}}$, $\boldsymbol{l_{zdi}}$ are the components of vector $\overrightarrow{O_sC_d}$ along axes o_sx_s, o_sy_s and o_sz_s respectively. In addition, $\boldsymbol{F_{xsi}}$, $\boldsymbol{F_{ysi}}$ and $\boldsymbol{F_{zsi}}$ are the forces from the force sensor which are parallel to axes o_sx_s, o_sy_s and o_sz_s respectively. $\boldsymbol{M_{xsi}}$, $\boldsymbol{M_{ysi}}$ and $\boldsymbol{M_{zsi}}$ are the torques exerted on the force sensor which are around the axes o_sx_s, o_sy_s and o_sz_s respectively. The angle between $\boldsymbol{F_{xyui}}$ and axis o_sx_s is named as θ_i which is in the range of $[-\pi, \pi]$. The angle between the axis of hole and peg is named as φ_i which is in the range of $[0, \pi/2)$. Likewisely, θ_i' denotes the angle between $\boldsymbol{F_{xydi}}$ and axis o_sx_s with range of $[-\pi, \pi]$. $\boldsymbol{e_{xs}}$, $\boldsymbol{e_{ys}}$ and $\boldsymbol{e_{zs}}$ are unit vector along axes o_sx_s, o_sy_s and o_sz_s respectively. h_t is the height of transmit component. r_h and r_p are the radius of hole and peg respectively. d_i is the distance from C_u to bottom of hole as shown in Fig. 2.

In the case of $\mathbf{S_1}$, contact force and friction force named as $\boldsymbol{N_{u1}}$ and $\boldsymbol{f_{u1}}$ respectively are exerted on the contact point C_{u1} of hole as shown in Fig. 2. The direction of $\boldsymbol{N_{u1}}$ is perpendicular to the axis of hole and parallel to the plane $o_sx_sy_s$. The direction of $\boldsymbol{f_{u1}}$ is parallel to the axis of hole. Thus, in the situation of $\mathbf{S_1}$, the output force and torque equations of force sensor is given as

$$\boldsymbol{F_{xs1}} = |\boldsymbol{N_{u1}}| \cos\theta_1 \boldsymbol{e_{xs}} \tag{4}$$

$$\boldsymbol{F_{ys1}} = |\boldsymbol{N_{u1}}| \sin\theta_1 \boldsymbol{e_{ys}} \tag{5}$$

$$\boldsymbol{F_{zs1}} = |\boldsymbol{f_{u1}}|\boldsymbol{e_{zs}} = \mu|\boldsymbol{N_{u1}}|\boldsymbol{e_{zs}} \tag{6}$$

$$M_{xs1} = \boldsymbol{l_{zu1}} \times \boldsymbol{F_{ys1}} + \boldsymbol{l_{yu1}} \times \boldsymbol{F_{zs1}} = (d_1 + h_t + r_h\mu)|\boldsymbol{N_{u1}}| \sin\theta_1 \boldsymbol{e_{xs}} \tag{7}$$

$$\boldsymbol{M_{ys1}} = \boldsymbol{l_{zu1}} \times \boldsymbol{F_{xs1}} + \boldsymbol{l_{xu1}} \times \boldsymbol{F_{zs1}} = -(d_1 + h_t + r_h\mu)|\boldsymbol{N_{u1}}| \cos\theta_1 \boldsymbol{e_{ys}} \tag{8}$$

$$M_{zs1} = 0 \tag{9}$$

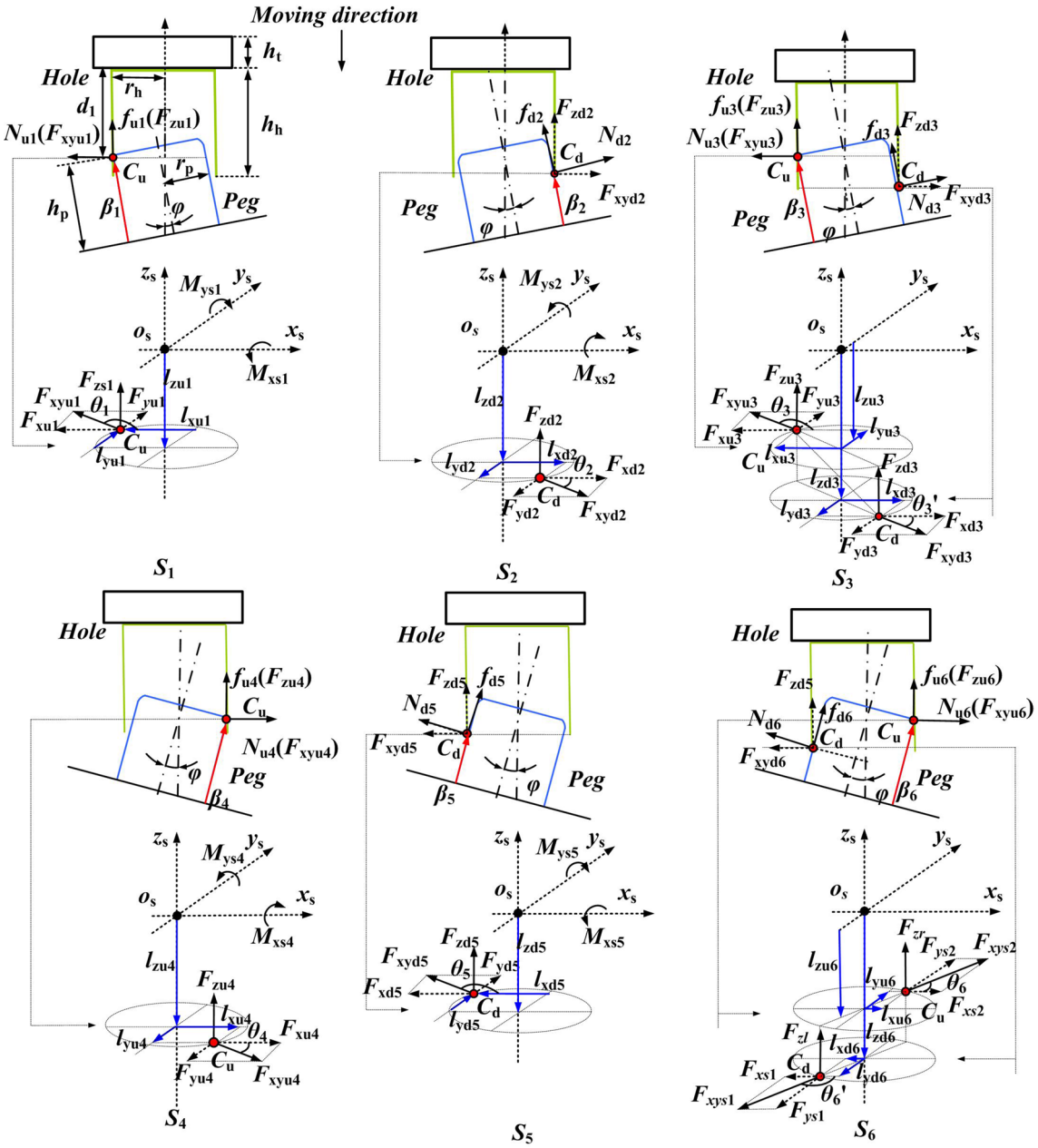

Fig. 2 Force and torque analysis for the insertion of peg and hole

where μ is coefficient of the friction force. $\boldsymbol{l_{xu1}}$, $\boldsymbol{l_{yu1}}$ and $\boldsymbol{l_{zu1}}$ are expressed as $\boldsymbol{l_{xu1}} = r_h \cos\theta_1 \boldsymbol{e_{xs}}$, $\boldsymbol{l_{yu1}} = r_h \sin\theta_1 \boldsymbol{e_{ys}}$ and $\boldsymbol{l_{zu1}} = -(d_1 + h_t)\boldsymbol{e_{zs}}$ respectively. It can be seen that, in the case of $\mathbf{S_1}$, the forces $\boldsymbol{F_{xsi}}$ and $\boldsymbol{F_{ysi}}$ or torque $\boldsymbol{M_{xs1}}$ and $\boldsymbol{M_{ys1}}$ are only related to the angle θ_1 from Eqs. (4), (5), (7) and (8). In addition, the output force and torque equations of force sensor in the case of $\mathbf{S_4}$ are same as $\mathbf{S_1}$.

Similarly, in the case of $\mathbf{S_2}$, contact force and friction force named as $\boldsymbol{N_{d2}}$ and $\boldsymbol{f_{d2}}$ respectively are exerted on the contact point C_{d2} of hole. To be different of the case of $\mathbf{S_1}$, the direction of $\boldsymbol{N_{d2}}$ is perpendicular to the axis of peg and the direction of $\boldsymbol{f_{d2}}$ is parallel to the axis of peg. Therefore, the resultant force of $\boldsymbol{N_{d2}}$ and $\boldsymbol{f_{d2}}$ can be divided into two component forces named as $\boldsymbol{F_{xyd2}}$ and $\boldsymbol{F_{zd2}}$ whose direction are parallel to the plane of $o_s x_s y_s$ and axis $o_s z_s$ respectively. The magnitude of $\boldsymbol{F_{xyd2}}$ and $\boldsymbol{F_{zd2}}$ can be calculated as

$$\left|\boldsymbol{F_{xyd2}}\right| = \left|\boldsymbol{N_{d2}}\right| \cos\varphi_2 - \left|\boldsymbol{f_{d2}}\right| \sin\varphi_2 = \left|\boldsymbol{N_{d2}}\right| g_1(\varphi_2) \tag{10}$$

$$|\boldsymbol{F}_{\mathbf{zd2}}| = |\boldsymbol{N}_{\mathbf{d2}}| \sin\varphi_2 + |\boldsymbol{f}_{\mathbf{d2}}| \cos\varphi_2 = |\boldsymbol{N}_{\mathbf{d2}}| \mathrm{g}_2(\varphi_2) \tag{11}$$

where $g_1(\varphi_2) = (\cos\varphi_2 - \mu \sin\varphi_2)$ and $\mathrm{g}_2(\varphi_2) = (\sin\varphi_2 + \mu\cos\varphi_2)$.

Then, the output force and torque equations of force sensor in the case of $\mathbf{S_2}$ are given by

$$\boldsymbol{F}_{\mathbf{xs2}} = \left|\boldsymbol{F}_{\mathbf{xyd2}}\right| \cos\theta_2' \boldsymbol{e}_{\mathbf{xs}} = |\boldsymbol{N}_{\mathbf{d2}}| \mathrm{g}_1(\varphi_2) \cos\theta_2' \boldsymbol{e}_{\mathbf{xs}} \tag{12}$$

$$\boldsymbol{F}_{\mathbf{ys2}} = \left|\boldsymbol{F}_{\mathbf{xyd2}}\right| \sin\theta_2' \boldsymbol{e}_{\mathbf{ys}} = |\boldsymbol{N}_{\mathbf{d2}}| \mathrm{g}_1(\varphi_2) \sin\theta_2' \boldsymbol{e}_{\mathbf{ys}} \tag{13}$$

$$\boldsymbol{F}_{\mathbf{zs2}} = |\boldsymbol{F}_{\mathbf{zd2}}| \boldsymbol{e}_{\mathbf{zs}} = |\boldsymbol{N}_{\mathbf{d2}}| \mathrm{g}_2(\varphi_2) \boldsymbol{e}_{\mathbf{zs}} \tag{14}$$

$$\begin{aligned} \boldsymbol{M}_{\mathbf{xs2}} &= \boldsymbol{l}_{\mathbf{zd2}} \times \boldsymbol{F}_{\mathbf{ys2}} + \boldsymbol{l}_{\mathbf{yd2}} \times \boldsymbol{F}_{\mathbf{zs2}} \\ &= [(h_{\mathrm{h}} + h_{\mathrm{t}}) \mathrm{g}_1(\varphi_2) + r_{\mathrm{h}} \mathrm{g}_2(\varphi_2)] |\boldsymbol{N}_{\mathbf{d2}}| \sin\theta_2' \boldsymbol{e}_{\mathbf{xs}} \end{aligned} \tag{15}$$

$$\begin{aligned} \boldsymbol{M}_{\mathbf{ys2}} &= \boldsymbol{l}_{\mathbf{zd2}} \times \boldsymbol{F}_{\mathbf{xs2}} + \boldsymbol{l}_{\mathbf{xd2}} \times \boldsymbol{F}_{\mathbf{zs2}} \\ &= -[(h_{\mathrm{h}} + h_{\mathrm{t}}) \mathrm{g}_1(\varphi_2) + r_{\mathrm{h}} \mathrm{g}_2(\varphi_2)] |\boldsymbol{N}_{\mathbf{d2}}| \cos\theta_2' \boldsymbol{e}_{\mathbf{ys}} \end{aligned} \tag{16}$$

$$\boldsymbol{M}_{\mathbf{zs2}} = 0 \tag{17}$$

where $\boldsymbol{l}_{\mathbf{xd2}}$, $\boldsymbol{l}_{\mathbf{yd2}}$ and $\boldsymbol{l}_{\mathbf{zd2}}$ can be calculated as $\boldsymbol{l}_{\mathbf{xd2}} = r_{\mathrm{h}} \cos\theta_2' \boldsymbol{e}_{\mathbf{xs}}, \boldsymbol{l}_{\mathbf{yd2}} = r_{\mathrm{h}} \sin\theta_2' \boldsymbol{e}_{\mathbf{ys}}$ and $\boldsymbol{l}_{\mathbf{zd2}} = -(h_{\mathrm{h}} + h_{\mathrm{t}}) \boldsymbol{e}_{\mathbf{zs}}$ respectively. Hence, from Eqs. (15) and (16) it can be seen that the forces $\boldsymbol{F}_{\mathbf{xs2}}$ and $\boldsymbol{F}_{\mathbf{ys2}}$ or the torque $\boldsymbol{M}_{\mathbf{xs2}}$ and $\boldsymbol{M}_{\mathbf{ys2}}$ are simultaneously related to the angle θ_2' and φ_2 which are different from the case $\mathbf{S_1}$. In addition, the output force and torque equations of force sensor in the case of $\mathbf{S_5}$ are same as $\mathbf{S_2}$.

For the case of $\mathbf{S_3}$ which is belong to the two-point contact type, the two contact points C_{u3} and C_{d3} are impacted by contact force and friction force named as $\boldsymbol{N}_{\mathbf{u3}}, \boldsymbol{f}_{\mathbf{u3}}, \boldsymbol{N}_{\mathbf{d3}}$ and $\boldsymbol{f}_{\mathbf{d3}}$ respectively. The direction of $\boldsymbol{N}_{\mathbf{u3}}$ and $\boldsymbol{N}_{\mathbf{d3}}$ are perpendicular to the axis of hole and peg respectively while direction of $\boldsymbol{f}_{\mathbf{u3}}$ and $\boldsymbol{f}_{\mathbf{d3}}$ are parallel to the axisof hole and peg respectively. Thus, the magnitude of $\boldsymbol{F}_{\mathbf{xyu3}}$, $\boldsymbol{F}_{\mathbf{zu3}}\boldsymbol{F}_{\mathbf{xyd3}}$ and $\boldsymbol{F}_{\mathbf{zd3}}$ can be calculated as

$$\left|\boldsymbol{F}_{\mathbf{xyu3}}\right| = |\boldsymbol{N}_{\mathbf{u3}}| \tag{18}$$

$$|\boldsymbol{F}_{\mathbf{zu3}}| = |\boldsymbol{f}_{\mathbf{u3}}| \tag{19}$$

$$\left|\boldsymbol{F}_{\mathbf{xyd3}}\right| = |\boldsymbol{N}_{\boldsymbol{d3}}|(\cos\varphi_3 - \mu \sin\varphi_3) = |\boldsymbol{N}_{\boldsymbol{d3}}| \mathrm{g}_1(\varphi_3) \tag{20}$$

$$|\boldsymbol{F}_{\mathbf{zd3}}| = |\boldsymbol{N}_{\mathbf{d3}}|(\sin\varphi_3 + \mu\cos\varphi_3) = |\boldsymbol{N}_{\mathbf{d3}}| \mathrm{g}_2(\varphi_3) \tag{21}$$

where $\mathrm{g}_1(\varphi_3) = (\cos\varphi_3 - \mu \sin\varphi_3)$ and $\mathrm{g}_2(\varphi_3) = (\sin\varphi_3 + \mu\cos\varphi_3)$.

$$\boldsymbol{F}_{\mathbf{xs3}} = \boldsymbol{F}_{\mathbf{xu3}} + \boldsymbol{F}_{\mathbf{xd3}} = [|\boldsymbol{N}_{\mathbf{u3}}| \cos\theta_3 + |\boldsymbol{N}_{\mathbf{d3}}| \mathrm{g}_1(\varphi_3) \cos\theta_3'] \boldsymbol{e}_{\mathbf{xs}} \tag{22}$$

$$\boldsymbol{F}_{\mathbf{ys3}} = \boldsymbol{F}_{\mathbf{yu3}} + \boldsymbol{F}_{\mathbf{yd3}} = [|\boldsymbol{N}_{\mathbf{u3}}| \sin\theta_3 + |\boldsymbol{N}_{\mathbf{d3}}| \mathrm{g}_1(\varphi_3) \sin\theta_3'] \boldsymbol{e}_{\mathbf{ys}} \tag{23}$$

$$\boldsymbol{F}_{\mathbf{zs3}} = \boldsymbol{F}_{\mathbf{zu3}} + \boldsymbol{F}_{\mathbf{zd3}} = [\mu|\boldsymbol{N}_{\mathbf{u3}}| + |\boldsymbol{N}_{\mathbf{d3}}| \mathrm{g}_2(\varphi_3)] \boldsymbol{e}_{\mathbf{zs}} \tag{24}$$

$$\begin{aligned} \boldsymbol{M}_{\mathbf{xs3}} &= \boldsymbol{l}_{\mathbf{zu3}} \times \boldsymbol{F}_{\mathbf{ys3}} + \boldsymbol{l}_{\mathbf{yu3}} \times \boldsymbol{F}_{\mathbf{zs3}} + \boldsymbol{l}_{\mathbf{zd3}} \times \boldsymbol{F}_{\mathbf{ys3}} + \boldsymbol{l}_{\mathbf{yd3}} \times \boldsymbol{F}_{\mathbf{zs3}} \\ &= h_{\mathrm{c1}} |\boldsymbol{N}_{\mathbf{u3}}| \sin\theta_3 \boldsymbol{e}_{\mathbf{xs}} + [h_{\mathrm{c2}} \mathrm{g}_1(\varphi_3) + r_{\mathrm{h}} \mathrm{g}_2(\varphi_3)] |\boldsymbol{N}_{\mathbf{d3}}| \sin\theta_3' \boldsymbol{e}_{\mathbf{xs}} \end{aligned} \tag{25}$$

$$\begin{aligned} \boldsymbol{M}_{\mathbf{ys3}} &= \boldsymbol{l}_{\mathbf{zu3}} \times \boldsymbol{F}_{\mathbf{xs3}} + \boldsymbol{l}_{\mathbf{xu3}} \times \boldsymbol{F}_{\mathbf{zs3}} + \boldsymbol{l}_{\mathbf{zd3}} \times \boldsymbol{F}_{\mathbf{xs3}} + \boldsymbol{l}_{\mathbf{xd3}} \times \boldsymbol{F}_{\mathbf{zs3}} \\ &= -h_{\mathrm{c1}} |\boldsymbol{N}_{\mathbf{u3}}| \cos\theta_3 \boldsymbol{e}_{\mathbf{ys}} - [h_{\mathrm{c2}} \mathrm{g}_1(\varphi_3) + r_{\mathrm{h}} \mathrm{g}_2(\varphi_3)] |\boldsymbol{N}_{\mathbf{d3}}| \cos\theta_3' \boldsymbol{e}_{\mathbf{ys}} \end{aligned} \tag{26}$$

$$\boldsymbol{M}_{zs3} = 0 \tag{27}$$

where $\boldsymbol{l}_{\mathbf{xu3}}$, $\boldsymbol{l}_{\mathbf{yu3}}$, $\boldsymbol{l}_{\mathbf{zu3}}$ $\boldsymbol{l}_{\mathbf{xd3}}$, $\boldsymbol{l}_{\mathbf{yd3}}$, $\boldsymbol{l}_{\mathbf{zd3}}$, h_{c1} and h_{c2} can be calculated as $\boldsymbol{l}_{\mathbf{xu3}} = r_h \cos\theta_3 \boldsymbol{e}_{\mathbf{xs}}, \boldsymbol{l}_{\mathbf{yu3}} = r_h \sin\theta_3 \boldsymbol{e}_{\mathbf{ys}}$, $\boldsymbol{l}_{\mathbf{zu3}} = -(d_3 + h_{\mathrm{t}}) \boldsymbol{e}_{\mathbf{zs}}$, $\boldsymbol{l}_{\mathbf{xd3}} = r_h \cos\theta_3' \boldsymbol{e}_{\mathbf{xs}}$, $\boldsymbol{l}_{\mathbf{yd3}} = r_h \sin\theta_3' \boldsymbol{e}_{\mathbf{ys}}$, $\boldsymbol{l}_{\mathbf{zd3}} = -(h_{\mathrm{h}} + h_{\mathrm{t}}) \boldsymbol{e}_{\mathbf{zs}}$, $h_{\mathrm{c1}} = d_3 + h_{\mathrm{t}} + r_{\mathrm{h}}\mu$, $h_{\mathrm{c2}} = h_{\mathrm{h}} + h_{\mathrm{t}}$ separately. Hence, from Eqs. (25) and (26) it can be seen that the forces $\boldsymbol{F}_{\mathbf{xs3}}$ and $\boldsymbol{F}_{\mathbf{ys3}}$ or the torque $\boldsymbol{M}_{\mathbf{xs3}}$ and $\boldsymbol{M}_{\mathbf{ys3}}$ are simultaneously related to the angle θ_3, θ_3' and φ_3. In addition, the output force and torque equations of force sensor in the case of $\mathbf{S_6}$ are same as $\mathbf{S_3}$.

Based on above analysis, two conclusions can be drawn as follows:

1. It is difficult to deduce which type of contact case the hole and peg should be belongs to in the process of insertion only based on the forces and torques from force sensors. Because no distinctive feature is existed on the force sensor's output equation between single point contact case and two-point contact case despite their calculation formula are different. In other word, one group of force sensor's output value may be corresponding to multiple contact cases.
2. For the contact case $\mathbf{S_1}$ or $\mathbf{S_4}$ which are attribute to single point contact case type, it can't be estimated the attitudes deviation from the force and torque equation because the forces $\boldsymbol{F}_{\mathbf{xsi}}$ and $\boldsymbol{F}_{\mathbf{ysi}}$ or torque $\boldsymbol{M}_{\mathbf{xsi}}$ and $\boldsymbol{M}_{\mathbf{ysi}}$ are only related to the angle θ_i ($i = 1$ or 4). Coupled with the problem of uncertain contact cases, it can't be obtained the pose deviation between the peg and hole directly only based on the forces and torques from force sensors. To overcome the above difficulties, we present a novel method to estimate the attitudes deviation between peg and hole in the following section.

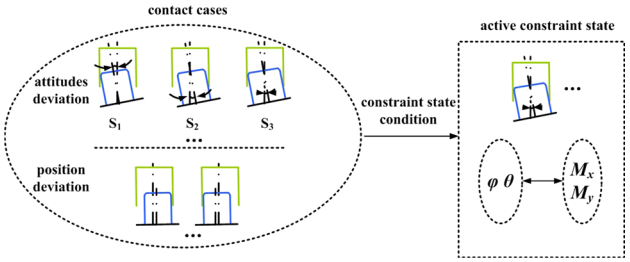

Fig. 3 The princple of the method for estimating the attitudes deviation from the force sensor based on active constraint state

2.3 The Method for Estimating the Attitude Deviation from the Force Sensor Based on Active Constraint State

Besides the contact states with attitudes deviation, the contact cases of the peg and hole also include the cases that only position deviation exists. Thus, in consideration of the above discussion, one can see that the contact case type should be certain before estimating the attitudes deviation. Hence, as shown in Fig. 3, the principle of our solution is to find a condition to force the peg and hole to be one certain contact state distinguishing from the kinds of contact states. We define the condition and the certain contact state as *constraint state condition* and *active constraint state* respectively. The *constraint state condition* is defined by the output forces of the micro force sensor and given as

$$\boldsymbol{F}_{\mathbf{xs}} = 0 \tag{28}$$

$$\boldsymbol{F}_{\mathbf{ys}} = 0 \tag{29}$$

Then, the *active constraint state* is defined as the contact state which satisfies the above constraint state condition. Specifically, the active constraint state must not be the case of position deviation and not be the single point contact case as well due to $\boldsymbol{F}_{\mathbf{xsi}}$ and $\boldsymbol{F}_{\mathbf{ysi}}$ are not be zero simultaneously in those cases. The active constraint state is confirmed be the special two-points contact case which satisfies the constraint condition at same time. In this case, the forces exerted on the hole can be given by

$$\boldsymbol{F}_{\mathbf{xyu}} = \boldsymbol{F}_{\mathbf{xyd}} \tag{30}$$

From the above equation combined with Eqs. (18)–(21), the following equations can be obtained as

$$|\boldsymbol{N}_{\mathbf{u}}| = |\boldsymbol{N}_{\mathbf{d}}|(\cos\varphi - \mu\sin\varphi) \tag{31}$$

$$\cos\theta = -\cos\theta' \tag{32}$$

$$\sin\theta = -\sin\theta' \tag{33}$$

Substituting the above equations into Eqs. (24)–(27), the remainder output force and torque equations of force sensor in the active constraint state are expressed as

$$\boldsymbol{F}_{\mathbf{zs}} = \boldsymbol{F}_{\mathbf{zu}} + \boldsymbol{F}_{\mathbf{zd}} = |\boldsymbol{N}_{\mathbf{d}}|[2\mu\cos\varphi + (1-\mu^2)\sin\varphi]\boldsymbol{e}_{\mathbf{zs}} \tag{34}$$

$$\begin{aligned}\boldsymbol{M}_{\mathbf{xs}} &= \boldsymbol{l}_{\mathbf{zu}} \times \boldsymbol{F}_{\mathbf{ys}} + \boldsymbol{l}_{\mathbf{yu}} \times \boldsymbol{F}_{\mathbf{zs}} + \boldsymbol{l}_{\mathbf{zd}} \times \boldsymbol{F}_{\mathbf{ys}} + \boldsymbol{l}_{\mathbf{yd}} \times \boldsymbol{F}_{\mathbf{zs}} \\ &= -[(h_{\mathrm{h}} - d)(\cos\varphi - \mu\sin\varphi) + (1+\mu^2)r_{\mathrm{h}}\sin\varphi]|\boldsymbol{N}_{\mathbf{d}}|\sin\theta\boldsymbol{e}_{\mathbf{xs}}\end{aligned} \tag{35}$$

$$\begin{aligned}\boldsymbol{M}_{\mathbf{ys}} &= \boldsymbol{l}_{\mathbf{zu}} \times \boldsymbol{F}_{\mathbf{xs}} + \boldsymbol{l}_{\mathbf{xu}} \times \boldsymbol{F}_{\mathbf{zs}} + \boldsymbol{l}_{\mathbf{zd}} \times \boldsymbol{F}_{\mathbf{xs}} + \boldsymbol{l}_{\mathbf{xd}} \times \boldsymbol{F}_{\mathbf{zs}} \\ &= [(h_{\mathrm{h}} - d)(\cos\varphi - \mu\sin\varphi) + (1+\mu^2)r_{\mathrm{h}}\sin\varphi]|\boldsymbol{N}_{\mathbf{d}}|\cos\theta\boldsymbol{e}_{\mathbf{ys}}\end{aligned} \tag{36}$$

$$\boldsymbol{M}_{\mathbf{zsi}} = 0 \tag{37}$$

where $h_{\mathrm{h}} - d = 2(r_{\mathrm{h}} - r_{\mathrm{p}}/\cos\varphi)\mathrm{ctg}\varphi$.

From Eq. (20), it can be concluded that the value of $\cos\varphi - \mu\sin\varphi$ is greater than or equal to zero. Furthermore, since φ is in range of [0, π/2), the value of $[(h_{\mathrm{h}} - d)(\cos\varphi - \mu\sin\varphi) + (1+\mu^2)r_{\mathrm{h}}\sin\varphi]$ is greater than or equal to zero too. Thus, from Eqs. (35) and (36), it can be found that the direction of $\boldsymbol{M}_{\mathbf{xs}}$ and $\boldsymbol{M}_{\mathbf{ys}}$ are decided by θ which is the angle between $\boldsymbol{F}_{\mathbf{xyu}}$ and axis $o_{\mathrm{s}}x_{\mathrm{s}}$. The attitudes deviation between peg and hole can be completely determined by the angles θ and φ.

Based on above analysis, two conclusions can be drawn as follows:

1. In the *active constraint state*, the direction of the toques $\boldsymbol{M}_{\mathbf{xsi}}$ and $\boldsymbol{M}_{\mathbf{ysi}}$ are decided by θ.
2. Equations (35) and (36) indicates that the toques $\boldsymbol{M}_{\mathbf{xsi}}$ and $\boldsymbol{M}_{\mathbf{ysi}}$ exerted on the hole can be controlled by adjusting the attitudes deviation and the relationship between them is nonlinear.

In summary, when the assembly is in the *active constraint state*, the attitude deviation between the peg and hole can be estimated by the torque information. On the other hand, the torque between the peg and hole can be controlled through the adjustment of the attitude difference. It should be pointed out that the same conclusions can be drawn for the case of the peg and hole are placed in the opposite direction using the same analytical method. Therefore, for the assembly of micro peg and hole, the problem of eliminating the attitudes difference can be converted to eliminate the torques exerted on them active constraint model. Based on this, the next part of the paper will introduce the control method based on force and torque information to realize the automatic assembly of peg and hole in detail.

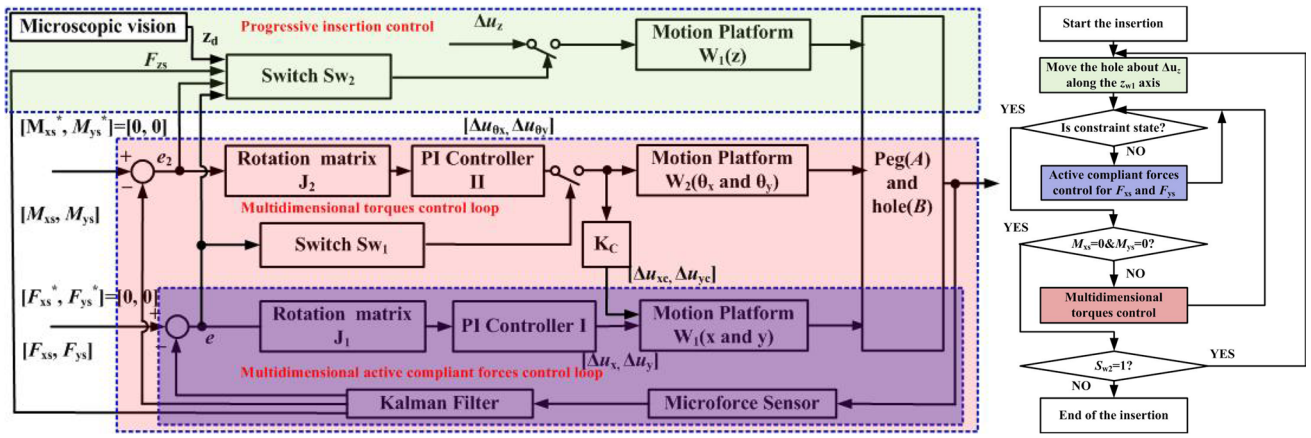

(a) Control system **(b)** Flow chart

Fig. 4 Control system for multi forces and toques based on active constraint state

3 The Automatic Assembly Control Method for Peg and Hole Based on Active Constraint State

In order to automatically assemble the peg and hole, and minimize the contact forces and torques in the meanwhile, the automatic control method based on active constraint state is designed. The main contribution of the method lies in making use of the active constraint state to eliminate the attitude deviation based on torque information. Thus, as shown in Fig. 4, the whole control system is mainly consists of three control loops as (1) Multidimensional active compliant forces control loop; (2) Multidimensional torques control loop; (3) Progressive insertion control.

To better explain the working principle of the designed control loops, the control flow chart is shown in Fig. 4b and illustrated as follows. When the insert operation begins, the motion along the axis of z_{w1} with a step of Δu_z is performed as the progressive insertion. The multidimensional active compliant forces control loop is designed to ensure the peg and hole be in the *active constraint state*. When F_{xs} and F_{ys} are zero, the control process goes into the step of multidimensional torque control loop. When M_{xs} and M_{ys} are not zero, the attitude deviation between the peg and hole exists which can be known from the above moment analysis. Thus, the module of multidimensional torque control is designed to eliminate the attitude deviation based on on M_{xs} and M_{ys}. At this time, it is necessary to further judge the F_{zs} and insertion depth named as d_{max} whether reached the threshold. If they do not reach the threshold, the control process goes into the step of progressive insertion. Otherwise, it indicated that the peg and hole had been assembled.

3.1 Multidimensional Active Compliant Forces Control Loop

Multidimensional active compliant forces control loop consists of rotation matrix $\boldsymbol{J_1}$, PI controller I, motion platform $\mathbf{W_1}$, microforce sensor and Kalman filter. The input of the control loop is two dimensional force error vector $\boldsymbol{e_1}$ and defined as

$$\boldsymbol{e}_1 = [\, F_{\mathrm{xs}} - F^*_{\mathrm{xs}} \;\; F_{\mathrm{ys}} - F^*_{\mathrm{ys}} \,]^T \tag{38}$$

where F_{xs} and F_{ys} are horizontal force exerted on $\boldsymbol{A}$ which are obtained from micro force sensor through Kalman filter. The rotation matrix $\boldsymbol{J}_1$ describes the rotation relationship between plane coordinate system $\mathrm{o_{w1}x_{w1}y_{w1}}$ and $\mathrm{o_sx_sy_s}$. Thus, the output of the PI controller I which is fed into the stepping motor of $\mathbf{W_1}$ is given as

$$[\Delta u_{\mathrm{x}}(\mathrm{k}),\ \Delta u_{\mathrm{y}}(\mathrm{k})]^{\mathrm{T}} = K_{\mathrm{P1}}\boldsymbol{J}_1(\boldsymbol{e}_1(\mathrm{k}) - \boldsymbol{e}_1(\mathrm{k}-1)) + K_{\mathrm{I1}}\boldsymbol{J}_1\boldsymbol{e}_1(\mathrm{k}) \tag{39}$$

where K_{P1} and K_{I1} are the proportional and integral coefficients of PI controller I respectively. $\boldsymbol{e}(\mathrm{k})$ and $\boldsymbol{e}(\mathrm{k}-1)$ represent the current forces error and forces error at instant k-1 accordingly. Thus, once the forces error had been controlled within specified range, the peg and hole is in the *active constraint state*.

3.2 Multidimensional Torques Control Loop

After peg and hole entering the *active constraint state*, it is necessary to eliminate attitude error between them based on torque information. To this end, a PI control system based on multidimensional torque information is designed which mainly includes the rotation matrix $\boldsymbol{J_2}$, PI controller II, motion platform $\mathbf{W_2}$, micro force sensor and Kalman filter. The error of torque vector at instant k is defined as

$$\boldsymbol{e}_2 = [\, M_{\mathrm{xs}}(\mathrm{k}) - M^*_{\mathrm{xs}} \;\; M_{\mathrm{ys}}(\mathrm{k}) - M^*_{\mathrm{ys}} \,]^T \tag{40}$$

where M_{xs} and M_{ys} are torques which are also obtained from micro force sensor through Kalman filter. The input of the PI controller II is torque vector through the rotation matrix $\boldsymbol{J_2}$ while its output is fed into the stepping motor of $\mathbf{W_2}$ to change the angles of the turning joints θ_x and θ_y. The control law can be expressed as

$$[\Delta u_{\theta x}(k),\ \Delta u_{\theta y}(k)]^T = K_{\mathrm{P2}}\boldsymbol{J}_2(\boldsymbol{e}_2(k) - \boldsymbol{e}_2(k-1)) + K_{\mathrm{I2}}\boldsymbol{J}_2\boldsymbol{e}_2(k) \tag{41}$$

where K_{P2} and K_{I2} are the proportional and integral coefficients of PI controller respectively. The rotation matrix $\boldsymbol{J_2}$ is utilized to estimate the rotation relationship between plane coordinate system $\mathrm{o_{w2}x_{w2}y_{w2}}$ and $\mathrm{o_s x_s y_s}$.

It is noted that the forces exerted on $\boldsymbol{A}$ will change due to the change of the plane position between the $\boldsymbol{A}$ and $\boldsymbol{B}$ when the output of PI controller II is fed into the stepping motor of $\mathbf{W_2}$. In order to make forces exerted on $\boldsymbol{A}$ not change rapidly, it is necessary to adjust the position of the hole $\boldsymbol{A}$ to make a rough compensation while adjusting the attitude of the $\boldsymbol{B}$. The amount of position compensation is calculated according to the attitude adjustment amount and given as

$$[\Delta u_{\mathrm{xc}}(\mathrm{k}),\ \Delta u_{\mathrm{yc}}(\mathrm{k})]^T = K_{\mathrm{C}}[\Delta u_{\theta x}(\mathrm{k}), \Delta u_{\theta y}(\mathrm{k})]^T \tag{42}$$

where K_{C} is the compensation coefficient obtained by off-line calibration. Nevertheless, the forces exerted on $\boldsymbol{A}$ may not be completely eliminated after rough position compensation. Then the multidimensional active compliant forces control loop is utilized to let $\boldsymbol{A}$ and $\boldsymbol{B}$ be active constraint state again.

3.3 Progressive Insertion Control

The progressive insertion control is relatively simple as it is only a switch control for the motion along the axis of z_{w1} with a step of Δu_z through the switch $\mathrm{S_{w2}}$. The condition of the switch $\mathrm{S_{w2}}$ is given as

$$s_{w2} = \begin{cases} 1 & F_{\mathrm{xs}} = F_{\mathrm{ys}} = 0, M_{\mathrm{xs}} = M_{\mathrm{ys}} = 0, d_z \le d_z^*, F_{zs} \le F_{zs}^* \\ 0 & F_{\mathrm{xs}} = F_{\mathrm{ys}} = 0, M_{\mathrm{xs}} = M_{\mathrm{ys}} = 0, (d_z > d_z^* \,||\, F_{zs} > F_{zs}^*) \end{cases} \tag{43}$$

where d_z is the insertion depth which can be obtained from microscopic vision. d_z^* and F_{zs}^* are the threshold of d_z and F_{zs} respectively. Note that once all the conditions are satisfied, the switch $\mathrm{S_{w2}}$ will be closed for the insertion operation. Otherwise, once insertion depth d_z or force F_{zs} is greater than their corresponding thresholds, the assembly ends immediately.

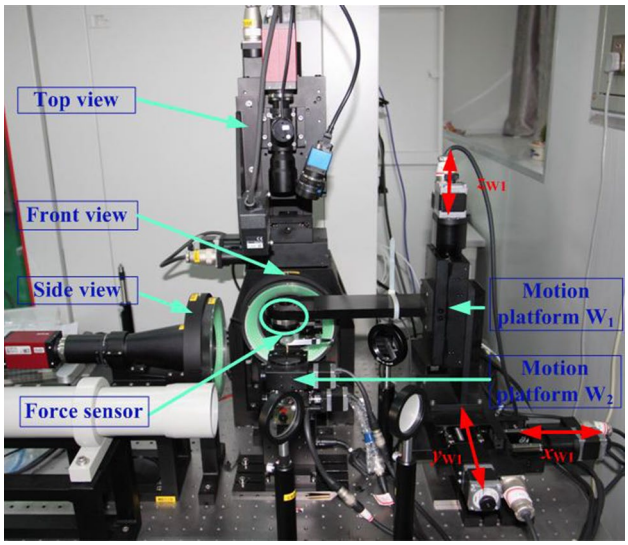

Fig. 5 The micro-assembly robot

Table 1 Parameters of controllers

Num	Controller parameter	Control period	Accuracy
1. Force control	$K_{\mathrm{P1}}=0.008$, $K_{\mathrm{I1}}=0.016$	0.6 s	0.05 N
2. Torque control	$K_{\mathrm{P2}}=0.03$, $K_{\mathrm{I2}}=0.09$	0.6 s	0.5 N mm

4 Experiment and Analysis

4.1 Experiment System Setup

In order to verify the proposed automatic assembly control method, the assembly of micro peg and hole was conducted on the micro-assembly robot as shown in Fig. 5. The robot is able to translate the hole $\boldsymbol{A}$ in 3 translational DOF by utilizing motion platform $\mathbf{W_1}$ whose axes are driven by Suruga's KS102 with the resolution of 1 μm. The peg $\boldsymbol{B}$ is fixed on 4-DOF motion platform $\mathbf{W_2}$ whose rotational axes are driven by Suruga's KAW06050 and KRW06360 with resolution of 0.01° and 0.03° respectively. Moreover, ATI's six-component micro force sensor Nano43 is employed to monitor the forces and torques whose resolution are 1/128 N and 1/20 N mm respectively. The range of forces and torques are given as ± 18 N and ± 250 N mm separately. To measure the position for the alignment of peg and hole, microscopic vision detection system are designed including three microscopic vision systems with their optic axis orthogonal reciprocally named as top view, front view, and side view respectively.

The outer diameter and height of the hole and the peg are given as 8.012 mm × 10.085 mm and

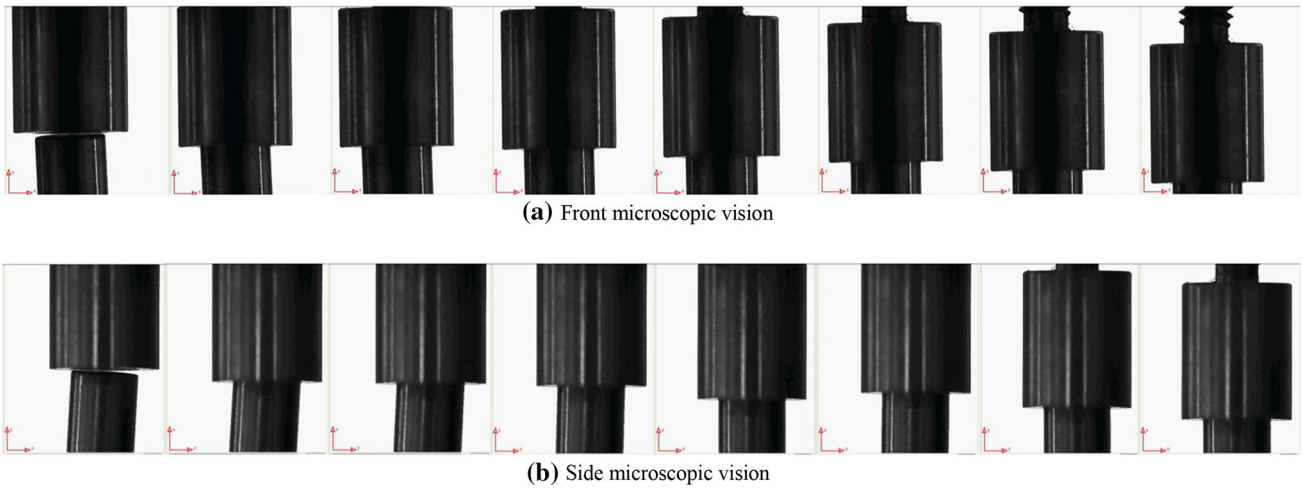

(a) Front microscopic vision

(b) Side microscopic vision

Fig. 6 Sequence snapshots of the automated micro-assembly

5.002 mm × 9.013 mm, respectively. The matching gap between the outer diameter of the peg and the inner diameter of the hole is 50um. Before the assembly begins, ***A*** and ***B*** are roughly aligned by using the front and side microscopic vision. In order to better verify the effect of forces and torques control, a certain attitude deviation between ***A*** and ***B*** is made in advance.

As given in Table 1, the control period of force and torque is 0.6 s. The proportional and integral coefficients of PI controller I are $K_{P1} = 0.08$ and $K_{I1} = 0.16$ respectively. The coefficients of torque controller are $K_{P2} = 0.03$ and $K_{I2} = 0.09$ respectively. Note that the rotation matrix $\boldsymbol{J_1}$ is approximated as identity matrix after calibration which implies that the axes $o_{w1}x_{w1}$ and $o_{w1}y_{w1}$ are substantially parallel to the axes o_sx_s and o_sy_s, respectively. Besides, the rotation matrix $\boldsymbol{J_2}$ is also approximated as identity matrix after calibration.

4.2 Experiment Result and Analysis

Figure 6 illustrates the process of an assembly experiment of ***A*** and ***B*** where the images of the upper part and the lower part are collected by the front microscopic vision and side microscopic vision respectively. Note that there is a certain height difference between the upper and lower parts of the image due to the installation deviation of the horizontal height of the front microscopic vision and side microscopic vision. It can be seen that the attitude difference exists between ***A*** and ***B*** before the assembly begins. The attitude deviation between ***A*** and ***B*** is eliminated after the adjustment of the position and attitude gradually. From Figs. 7, 8, 9, and 10, the six dimension force and torque which produced in an assembly experiment and the output of controllers are given.

Figure 7 illustrates the force exerted on the hole ***A*** in an assembly experiment measured by force sensor. According to the control strategy shown in Fig. 4, at the beginning of the assembly, the F_{xs} and F_{ys} are basically zero because the peg and hole do not touch each other. Meanwhile, as shown in Fig. 8, M_{xs} and M_{ys} are also basically zero. The motion along the axis of z_{w1} with a step of Δu_z is implemented continuously. Until about 17.6 s, when the peg and hole began to contact, the hole ***A*** began to be affected by the contact force and the torque was generated. At this moment, the peg and hole are still in the active constraint state since F_{xs} and F_{ys} are below the threshold. However, M_{xs} and M_{ys} exceed the threshold level. Hence, it is necessary to adjust the attitudes between ***A*** and ***B*** according to the amplitude and direction of M_{xs} and M_{ys}. Figure 10 gives the curve of the attitude adjustment control output of ***B*** in the whole assembly process. Note that the change of ***B***'s attitude will cause the plane position between peg and hole change. In order to make the force exerted on ***A*** do not change sharply due to the attitude adjustment of ***B***, the position of ***A*** needs to be adjusted for rough compensation when ***B***'s attitudes is adjusted. Figure 9 illustrates the curve of position adjustment control output named as Δu_x and Δu_y.

After the rough adjustment of ***A***'s position, the force F_{xs}, F_{ys}, M_{xs} and M_{ys} are all below the threshold and ***A*** needs to be inserted by exerting the control amount u_z along the axis $o_{w1}z_{w1}$. At the next moment of 19.2 s, M_{xs} and M_{ys} are still exceeds the threshold, so it is necessary to further adjust the attitude of ***B***. After two adjustments periods, F_{xs}, F_{ys}, M_{xs} and M_{ys} are in the threshold range, and then ***A*** continues to be inserted.

To further validate the performance of the proposed control method, we will analyze the change of forces and torques

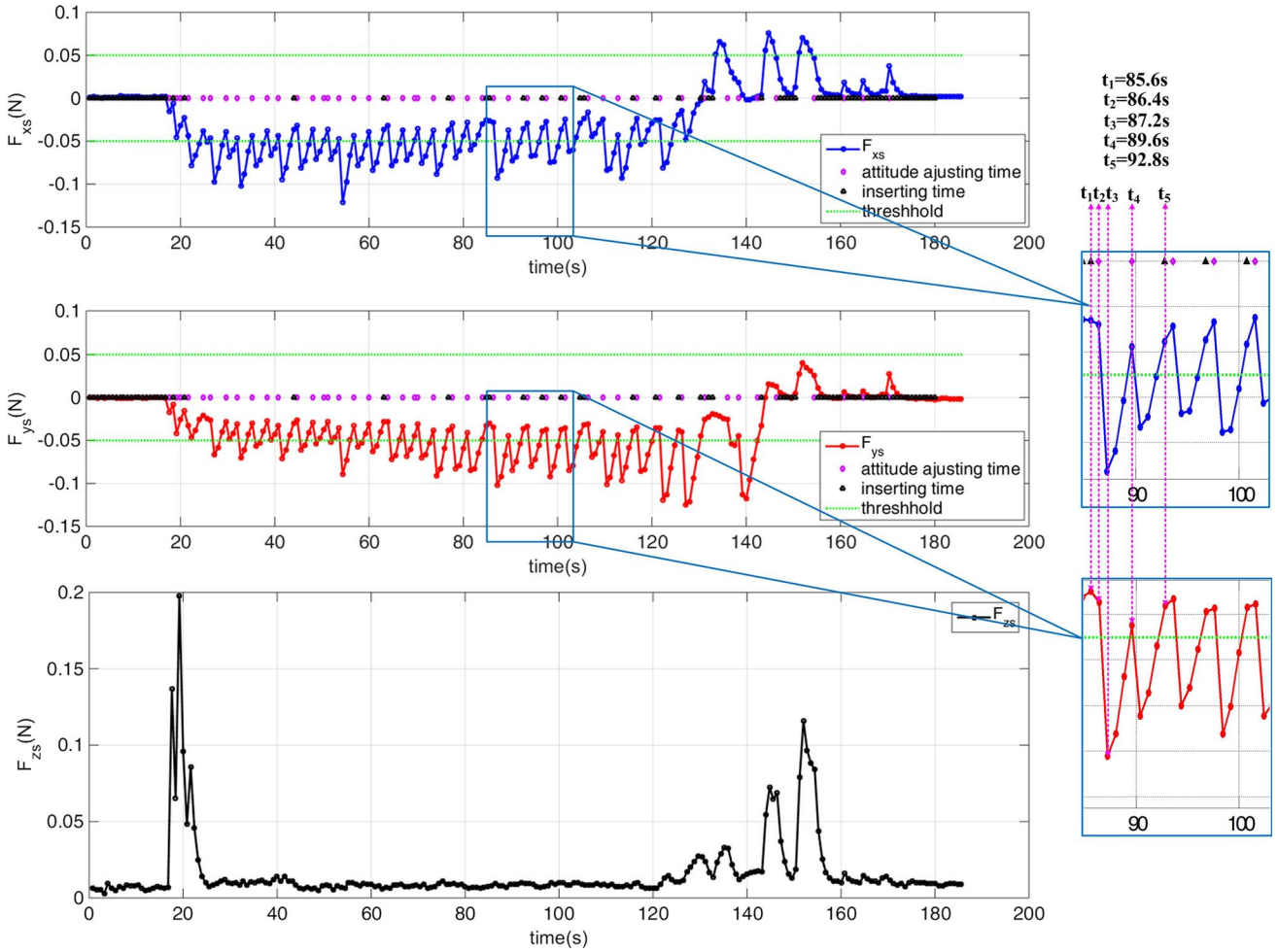

Fig. 7 The force curve of the hole ***A*** in an assembly experiment

in detail from $t_1 = 85.6$ s to $t_5 = 92.8$ s. When $t_1 = 85.6$ s, as shown in Figs. 7 and 8, F_{xs}, F_{ys}, M_{xs} and M_{ys} are below the threshold and ***A*** continues to be inserted along axis $o_{w1}z_{w1}$. At the next time $t_2 = 86.4$ s, ***A*** is still in the active constraint state and the control process goes into the step of multidimensional torque control. The two dimensional torque controller II is utilized to control the posture of ***B***. As shown in Fig. 10, the output of controller II named as $\Delta u_{\theta x}$ and $\Delta u_{\theta y}$ are fed into the stepping motor of $\mathbf{W_2}$ to change the angles of the turning joints θ_x and θ_y. At the same time, as shown in Fig. 9, the output of controller I named as Δu_x and Δu_y are fed into the stepping motor of W_1 to apply rough compensation. However, the above, rough compensation does not completely eliminate the position difference between the ***A*** and ***B*** caused by the attitude adjustment. Thus, as shown in Fig. 7, F_{xs} and F_{ys} are beyond the threshold range when $t_3 = 87.2$ s. In this case, ***A*** is not in the active constraint state and the controller I is used to carry out two dimensional force control. Through the force change curve from t_3 to t_4 shown in Fig. 7, the controller I is proved to have good performance of controlling the error of F_{xs} and F_{ys} within 0.05 N. Then, the control process enters the two-dimensional torque control state at instant t_4.

As shown in Figs. 7 and 8, from t_1 to t_5, the assembly process has undergone two dimensional force control and two dimensional torque control sequence. In the case of F_{xs}, F_{ys}, M_{xs} and M_{ys} were all within the threshold range, the next insert operation is performed at the t_5 instant. Similar to the process of t_1 to t_5, F_{xs}, F_{ys}, M_{xs} and M_{ys} have maintained a low level in the whole assembly process due to employment of our control strategy. Thus the compliance of the assembly is guaranteed. It is noted that there is a similar and specific pattern in two plots in Fig. 10. The shape of the two plots is determined by the error of torque vector and the rotation matrix $\boldsymbol{J_2}$ according to the control law given in Eq. (41). Since the rotation matrix $\boldsymbol{J_2}$ is approximated as

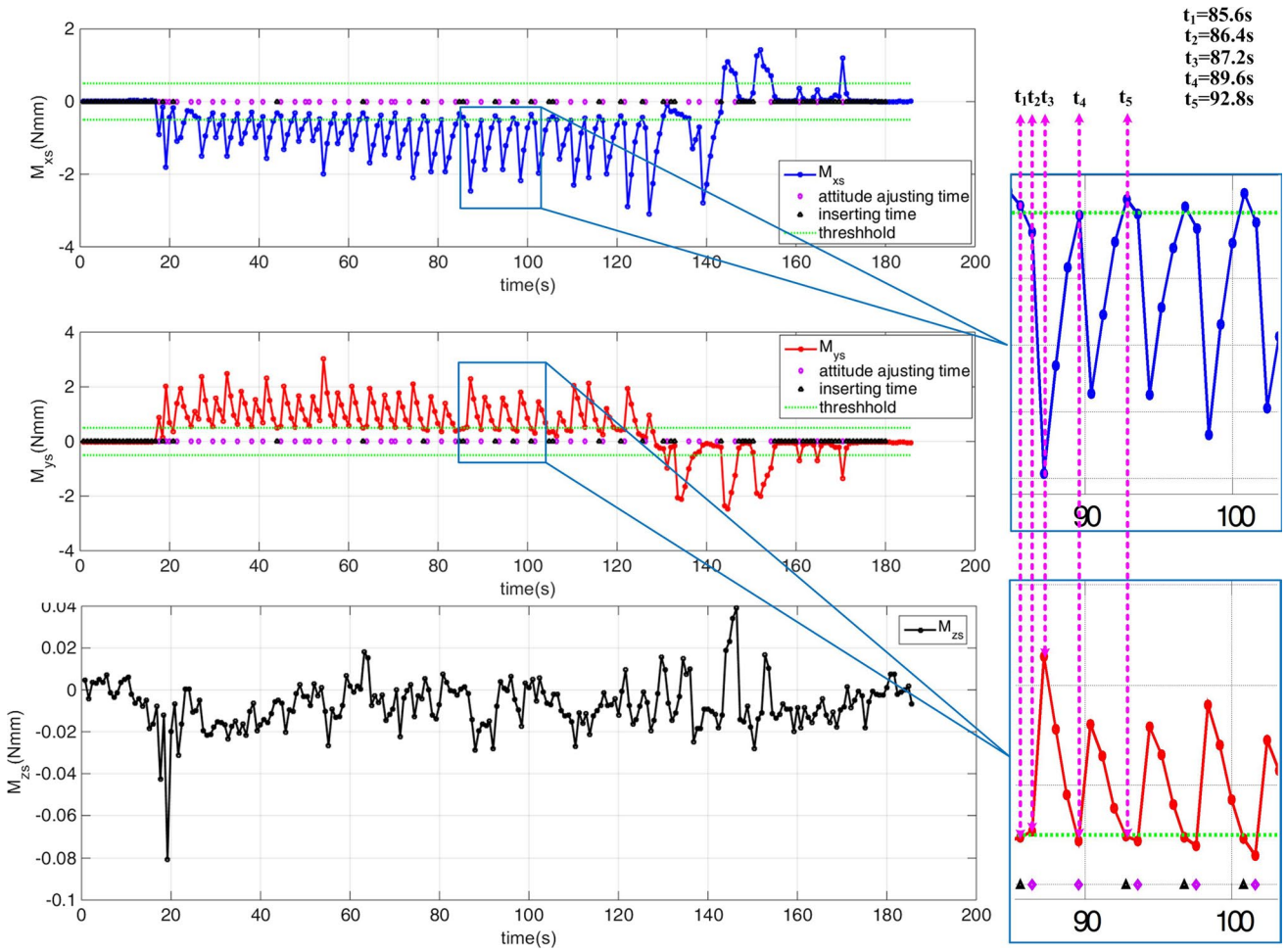

Fig. 8 The moment curve of the hole ***A*** in an assembly experiment

identity matrix after calibration, the similarity of the two plots in Fig. 10 is related to curve similarity between M_{xs} and M_{ys} in Fig. 8.

In addition, through the force change of F_{zs} in Fig. 7, we can see that F_{zs} has also maintained a very low level in the whole assembly process. Moreover, through the change curve of M_{zs} shown in Fig. 8, we can see that M_{zs} is near zero during the whole assembly process, which further validates the rationality of the model established in this paper. Figure 11 shows the trajectory of the hole ***A*** in the assembly process. It can be seen that the assembly is a progressive insertion process accompanying with the adjustment of the horizontal position. From this point of view, our control strategy imitates human's assembly experience to some extent.

To further validate the robust of the proposed method, twenty five times assembly tasks with varying initial attitude deviation between peg and hole are implemented, and 24 assembly attempts are successful, giving a success rate of 96%. To illustrate the advantage of the proposed method, the control results are compared to the control method in [17] which only uses the three dimensional force information. Its insertion control strategy is to reduce the horizontal forces by adjusting the position difference with a fixed step when the horizontal force exceeds the threshold value. Ten times assembly tasks with varying initial attitude deviation between peg and hole are implemented. Only three assembly attempts are successful whose initial attitude deviation are less than 0.8°. Noted that the initial attitude deviation is measured by front and side microscopic vision. The other seven assembly experiments failed because of blocking. Moreover, the larger the attitude deviation, the smaller the insertion depth of the blocking. The experimental results show that the limitation of the method in [17] lies in the

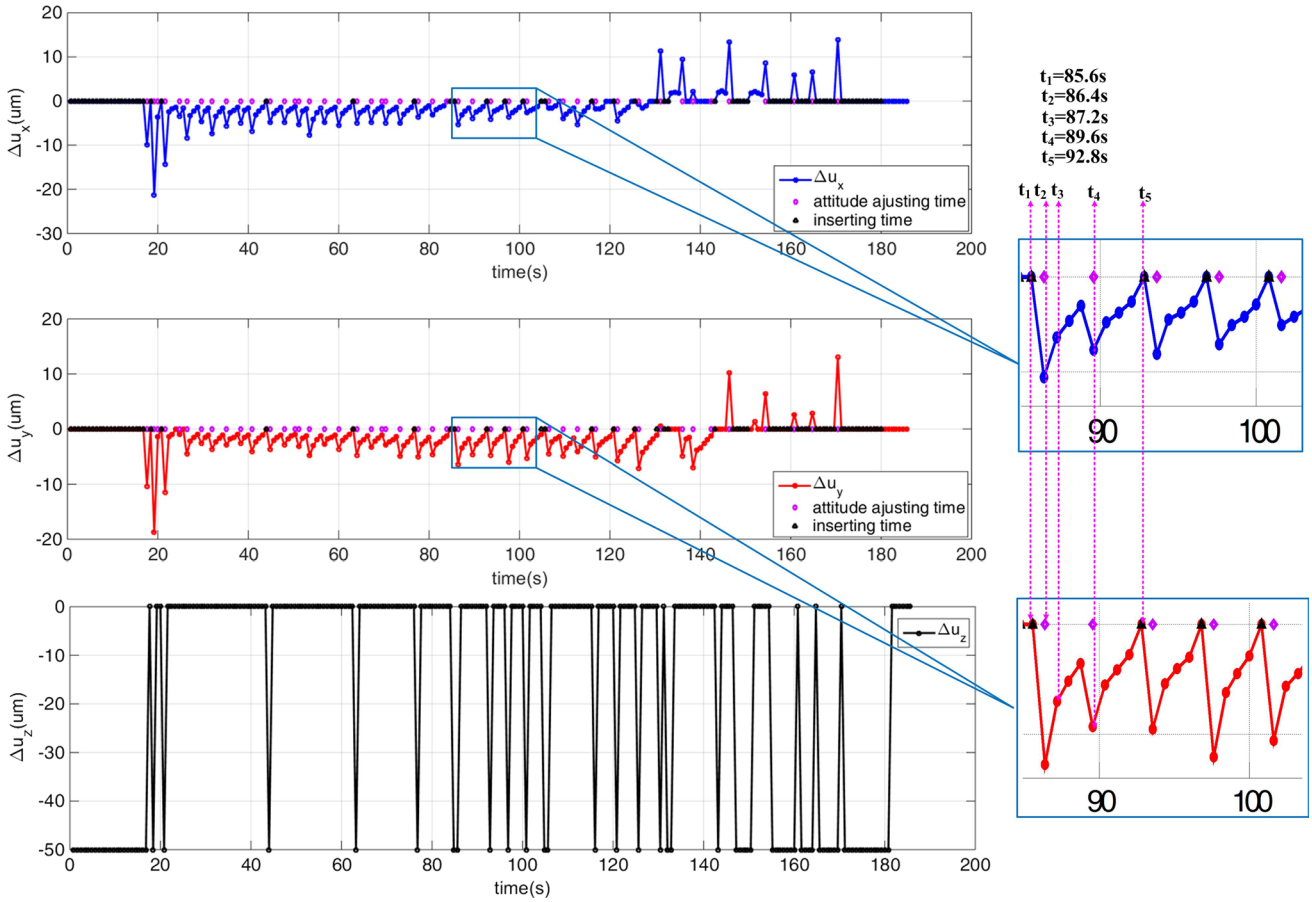

Fig. 9 The curve of position adjustment control output in an assembly experiment

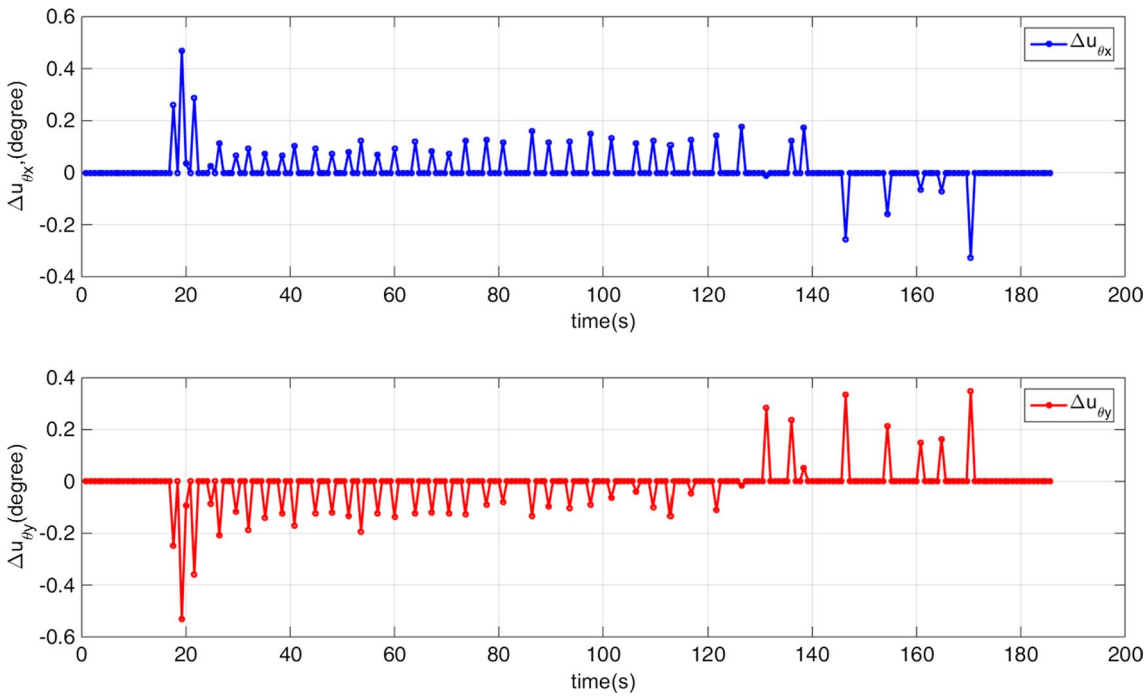

Fig. 10 The curve of attitude adjustment control output in an assembly experiment

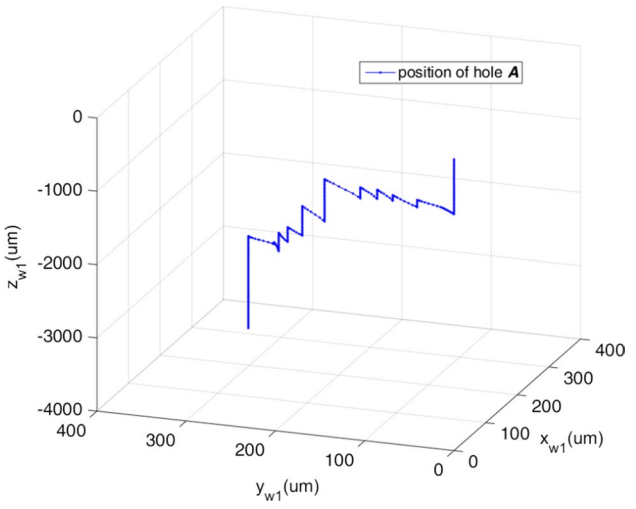

Fig. 11 The trajectory of the hole ***A*** in the assembly process

high accuracy requirement for the initial attitude deviation difference between peg and hole. In contrast, our proposed method has been proved that can be well adapted to the situation of attitude deviation due to the reasonable use of moment information.

In summary, the assembly task for peg and hole in this paper involves both multidimensional forces and torques control for the elimination of position and attitude deviation. The force and torque curves obtained in the experiments have demonstrated that the proposed two dimensional force and two dimensional torque control method can meet the precision requirements well, and the control accuracy of the forces and torques are 0.05 N and 0.5 Nmm respectively. Meanwhile, the maximum contact forces and torques in the whole assembly process are controlled within 0.15N and 3Nmm respectively which met and lossless assembly requirements.

5 Conclusions

An automatic assembly method for peg and hole insertion based on multidimensional micro forces and torques is studied through this paper. A novel method is proposed to estimate the deviation angles between the peg and the hole through the toques exerted on the sensors. A control strategy for controlling the horizontal contact forces and torques during the insertion process is presented to achieve automated insertion of peg and hole by eliminating the position and attitudes deviation interactively. Experiments conducted on the micro-assembly robot demonstrate the effectiveness of the proposed method and the assembly tasks were performed with the following accuracy: 50mN for force error and 0.5Nmm for the torque error. Future work will concern the assembly of flexible micro peg and hole with shrink fit requirement based on micro force and micro torque.

Acknowledgements This research is supported by National Natural Science Foundation of China under Grant 61503378, 61473293, 61803354, Science Challenge Project, No. 0006, and Foundation of Laboratory of Precision Manufacturing Technology CAEP under Grant ZD17003.

References

1. Brussel, H., & Peirs, J. (2000). Assembly of microsystems. *CIRP Annals—Manufacturing Technology, 49*(2), 451–472.
2. Fluitman, J. (1996). Microsystems technology: objectives. *Sensors and Actuators A: Physical, 56,* 151–166.
3. Kim, J. (2011). Visually guided 3D micro positioning and alignment system. *International Journal of Precision Engineering and Manufacturing, 12*(5), 797–803.
4. Li, F., Xu, D., Zhang, Z., Shi, Y., & Shen, F. (2014). Pose measuring and aligning of a micro glass tube and a hole on the micro sphere. *International Journal of Precision Engineering and Manufacturing, 15*(12), 2483–2491.
5. Thompson, J., & Fearing, R. (2001). Automating microassembly with ortho-tweezers and force sensing. In *IEEE international conference on intelligent robots and systems* (pp. 1327–1334). Maui, HI, USA: IEEE.
6. Tanikawa, T., Kawai, M., Koyachi, N., Arai, T., Ide, T., Kaneko, S., Ohta, R., & Hirose, T. (2001). Force control system for autonomous micro manipulation. In *IEEE International conference on robotics and automation* (pp. 610–615). Seoul, Korea: IEEE.
7. Kim, K., Liu, X., Zhang, Y., & Sun, Y. (2008). Nanonewton force-controlled manipulation of biological cells using a monolithic MEMS microgripper with two-axis force feedback. *Journal of Micromechanics and Microengineering, 18,* 1–8.
8. Xu, Q. (2013). Precision position/force interaction control of a piezo-electric multimorph microgripper for microassembly. *IEEE Transactions on Automation Science and Engineering, 10*(3), 503–514.
9. Xu, Q. (2013). Adaptive discrete-time sliding mode impedance control of a piezoelectric microgripper. *IEEE Transactions on Robotics, 29*(3), 663–673.
10. Komati, B., Rabenorosoa, K., Clevy, C., & Lutz, P. (2013). Automated guiding task of a flexible micropart using a two-sensing-finger microgripper. *IEEE Transactions on Automation Science and Engineering, 10*(3), 515–524.
11. Zhou, Y., Nelson, B., & Vikramaditya, B. (1998). Fusing force and vision feedback for micromanipulation. In *IEEE international conference on robotics and automation* (pp. 1220–1225). Leuven, Belgium: IEEE.
12. Lu, Z., & Chen, P. (2006). A force-feedback control system for micro-assembly. *Journal of Micromechanics and Microengineering, 16,* 1861–1868.
13. Shen, Y., Xi, N., & Li, W. (2003). Force-guided assembly of micro mirrors. In *IEEE international conference on intelligent robots and systems* (pp. 2149–2154). Las Vegas, USA: IEEE.
14. Li, Y., Zhang, Z., Ye, X., & Chen, S. (2016). A novel micro-assembly method based on the mapping between assembly force and position. *International Journal of Advanced Manufacturing Technology, 86,* 227–236.
15. Qin, F., & Xu, D. (2017). An active radial compliance method with anisotropic stiffness learning for precision assembly.

International Journal of Precision Engineering and Manufacturing, 18(4), 471–478.
16. Xu, Q. (2018). *Micromachines for biological micromanipulation*. Cham: Springer.
17. Liu, S., Xu, D., Zhang, D., & Zhang, Z. (2016). High precision automatic assembly based on microscopic vision and force information. *IEEE Transactions on Automation Science and Engineering, 13*(1), 382–393.
18. Kim, J., Yoon, H., & Ahn, S. (2013). Effect of repeated insertions into a mesoscale pinhole assembly: Case of interference fit. *International Journal of Precision Engineering and Manufacturing, 14*(9), 1651–1654.
19. Kim, Y., Song, H., & Song, J. (2014). Hole detection algorithm for chamferless square peg-in-hole based on shape recognition using F/T sensor. *International Journal of Precision Engineering and Manufacturing, 15*(3), 425–432.
20. Lee, W., & Kang, B. (2003). Micropeg manipulation with a compliant microgripper. In *Proceeding of IEEE international conference on robotics & automation*, Taipei, Taiwan, China, September 14–19 (pp. 3213–3218).
21. Zhang, J., & Wu, W. (2015). Interference fit assembly of microparts based on microscopic vision and force. *Key Engineering Materials, 645–646,* 1016–1023.

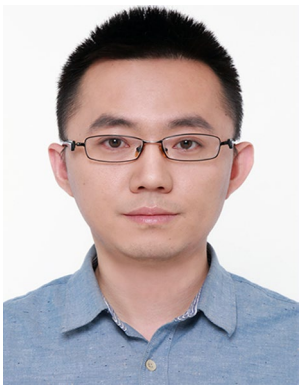

Fei Shen received received the B.Sc. and M.Sc. degrees from Xidian University, Xi'an, China, and Beijing Institute of Technology, Beijing, China, in 2007 and 2009, respectively, and the Ph.D. degree in control science and engineering from IACAS, Beijing, China, in 2012. He is currently an Associate Professor in the Research Center of Precision Sensing and Control, IACAS. His research interests include robot control, robot vision control and micro-assembly.

Zhengtao Zhang received the B.Sc. and M.Sc. degrees from China University of Petroleum, Dongying, China, and Beijing Institute of Technology, Beijing, China, in 2004 and 2007, respectively, and the Ph.D. degree in control science and engineering from IACAS, Beijing, China, in 2010. He is currently a Professor in the Research Center of Precision Sensing and Control, IACAS. His research interes ts include visual measurement, micro-assembly and automation.

De Xu received the B.Sc. and M.Sc. degrees from the Shandong University of Technology, Jinan, China, in 1985 and 1990, respectively, and the Ph.D. degree from Zhejiang University, Hangzhou, China, in 2001, all in control science and engineering. He has been with IACAS since 2001. He is currently a Professor with the Research Center of Precision Sensing and Control, IACAS. His current research interests include robotics and automation such as visual measurement and control, microscopic vision, and micro-assembly.

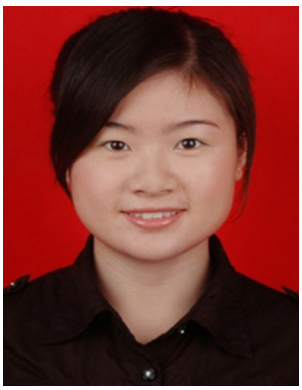

Juan Zhang received the B.Sc. and M.Sc. degrees from the Zhengzhou University, Zhengzhou, China, in 2007 and 2010, and the Ph.D. degree in control science and engineering from IACAS, Beijing, China, in 2013. She is currently an Associate Professor in the Research Center of Laser Fusion, China Academy of Engineering Physics. Her research interests include machine vision, robot control, and micro-assembly.

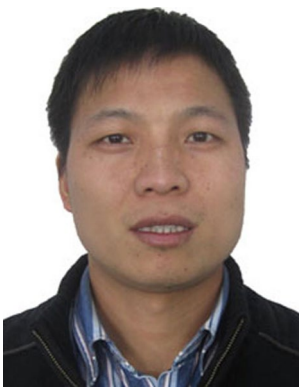

Wenrong Wu received the B.S. degree in mechanical design and manufacturing from Chongqing University, Chongqing, China, in 2000, and the M.S. degree in mechanical and electrical engineering from the University of Electronic Science and Technology, Chengdu, China, in 2006. He is currently a Vice Professor at the Laser Fusion Research Center and Laboratory of Precision Manufacturing Technology, Chinese Academy of Engineering Physics (CAEP), Mianyang, China. His current research interests include design of electromechanical integration, especially the control of microassembly robot.